

Effects of CsSnxPb1-xI3 Quantum Dots as Interfacial Layer on Photovoltaic Performance of Carbon-Based Perovskite Solar Cells

Chi Zhang

Wuhan University of Technology

Zhiyuan He

Wuhan University of Technology

Xuanhui Luo

Wuhan University of Technology

Rangwei Meng

Wuhan University of Technology

Mengwei Chen

Wuhan University of Technology

Haifei Lu

Wuhan University of Technology

yingping yang (✉ ypyang@whut.edu.cn)

"Wuhan University of Technology" <https://orcid.org/0000-0002-4183-674X>

Nano Express

Keywords: Tin-doped perovskite quantum dots, photovoltaic performance, carbon-based perovskite solar cells

Posted Date: February 16th, 2021

DOI: <https://doi.org/10.21203/rs.3.rs-196729/v1>

License: © ⓘ This work is licensed under a Creative Commons Attribution 4.0 International License.

[Read Full License](#)

1 **Effects of CsSn_xPb_{1-x}I₃ quantum dots as interfacial layer on photovoltaic**
2 **performance of carbon-based perovskite solar cells**

3 Chi Zhang, Zhiyuan He, Xuanhui Luo, Rangwei Meng, Mengwei Chen, Haifei Lu and
4 Yingping Yang*

5 *correspondence: ypyang@whut.edu.cn

6 Department of Physics, School of Science, Wuhan University of Technology, Wuhan 430070,
7 P. R. China

8

9 **Abstract**

10 In this work, inorganic tin-doped perovskite quantum dots (PQDs) are incorporated into carbon-
11 based perovskite solar cells (PSCs) to improve their photovoltaic performance. On the one hand,
12 by controlling the content of Sn²⁺ doping, the energy level of the tin-doped PQDs can be
13 adjusted, to realize optimized band alignment and enhanced separation of photogenerated
14 electron-hole pairs. On the other hand, the incorporation of tin-doped PQDs provided with a
15 relatively high acceptor concentration due to the self-p-type doping effect, is able to reduce the
16 width of the depletion region near the back surface of the perovskite, thereby enhancing the
17 hole extraction. Especially, after the addition of CsSn_{0.2}Pb_{0.8}I₃ QDs, improvement of the power
18 conversion efficiency (PCE) from 12.80% to 14.22% can be obtained, in comparison to the
19 pristine device. Moreover, the experimental results are analyzed through the simulation of the
20 one-dimensional perovskite/tin-doped PQDs heterojunction.

21 **Keywords:** Tin-doped perovskite quantum dots, photovoltaic performance, carbon-based
22 perovskite solar cells

1 **Introduction**

2 In past few years, perovskite materials have been widely applied in solar cells due to their
3 excellent electrical and optical properties, such as suitable bandgap width, large light absorption
4 coefficient and good defect tolerance [1-6]. Interface engineering, as a strategy to modify the
5 interface characteristics of thin film devices, has become one of the approaches to improve the
6 performance of perovskite solar cells (PSCs) [7,8]. Recently, lead-based halide perovskite
7 quantum dots (PQDs) in the form of $APbX_3$ ($A = CH_3NH_3^+$ (MA^+), Cs^+ ; $X = Cl^-$, Br^- , I^-) are
8 often used as interfacial layers or additives for optimized band alignment thanks to their
9 adjustable band structures [9-15]. The combination of perovskite absorbers and PQDs is
10 regarded as an effective method for enhanced charge extraction and improved PSC properties.

11 It is worth noting that most of the relevant researches are based on PSCs with hole-
12 transporting layers (HTLs). But in recent years, carbon-based HTL-free PSCs with simple
13 preparation processes and low costs have been given much attention [16-18]. Similarly, PQDs
14 can also be used in this PSC structure. However, some other requirements besides band
15 alignment should be taken into consideration. First, the lattice structures of lead-based PQDs
16 are not very stable due to Pb^{2+} with a large ionic radius reducing the tolerance factor. Therefore,
17 lead-reduced PQDs are promising candidates. Second, because of the lack of HTLs, the hole
18 transport performance is bound to be weakened. Consequently, the added PQDs are required to
19 supply extra free holes, so that photogenerated holes can be smoothly transferred from the
20 perovskite layer to the carbon electrode.

21 The ion exchange method using metal cations with smaller ionic radii (such as Cu^{2+} , Zn^{2+} ,
22 Sn^{2+} , Cd^{2+}) to partially replace Pb^{2+} has been proven to improve the lattice stability of PQDs

1 [19-21]. Among these metal cations, Sn^{2+} is easily to oxidize to Sn^{4+} , which can introduce self-
2 p-type doping effects to enhance hole transfer [22-24]. Especially, Liu et al. synthesized
3 $\text{CsSn}_{0.6}\text{Pb}_{0.4}\text{I}_3$ QDs featuring a hole mobility of $40.12 \text{ cm}^2 \text{ V}^{-1} \text{ s}^{-1}$ and good stability in the
4 ambient air [25]. Xu and co-workers incorporated $\text{CsSnBr}_{3-x}\text{I}_x$ QDs between the CsPbBr_3
5 perovskite and the carbon electrode to promote charge extraction [26]. Very recently, Duan et
6 al. found that $\text{MAPbI}_3/\text{CsSnI}_3$ heterojunction as the light-harvester in the carbon-based HTL-
7 free PSC could facilitate the hole transfer [27]. Inspired by these above, we propose that tin-
8 doped PQDs with appropriate energy levels and self-p-type doping effects are able to function
9 like HTLs to modify the injection and transport characteristics of holes.

10 In this work, tin-doped PQDs in the form of $\text{CsSn}_x\text{Pb}_{1-x}\text{I}_3$ were incorporated between the
11 MAPbI_3 perovskite and the carbon electrode to achieve optimized band alignment and
12 improved hole transfer. An increment in power conversion efficiency (PCE) of 11.09%, from
13 12.80% to 14.22%, could be obtained after the addition of $\text{CsSn}_{0.2}\text{Pb}_{0.8}\text{I}_3$ QDs.

14

15 **Methods**

16 **Materials**

17 Tin iodide (SnI_2 ; 99.99%) was bought from Youxuan technology (China). Cesium carbonate
18 (Cs_2CO_3 ; 99%), 1-octadecene (ODE; >90%), oleic acid (OA; 99%), oleylamine (OAM; 80%-
19 90%), methyl acetate (MeOAc; 98%) and trioctylphosphine (TOP; 90%) were purchased from
20 Macklin (China). Lead iodide (PbI_2 ; 99.99%) and methylammonium iodide (MAI; 99.5%) were
21 obtained from Xi'an p-OLED (China). Titanium diisopropoxide bis (acetylacetonate; 75%),
22 dimethylsulfoxide (DMSO; 99.9%) and N,N-dimethylformamide (DMF; 99.8%) were

1 purchased from Sigma-Aldrich (US). The TiO₂ paste (30NR-D) and the low-temperature
2 carbon electrode paste were obtained from Shanghai MaterWin New Materials (China).

3

4 **Synthesis and purification of tin-doped PQDs**

5 We adopted a simple mixed-heating procedure to synthesize tin-doped PQDs. Briefly, Cs₂CO₃,
6 SnI₂ and PbI₂ with a specific molar ratio (CsSn_{0.1}Pb_{0.9}I₃ QDs: 0.037 mmol Cs₂CO₃, 0.2 mmol
7 PbI₂, 0.15 mmol SnI₂; CsSn_{0.2}Pb_{0.8}I₃ QDs: 0.037 mmol Cs₂CO₃, 0.2 mmol PbI₂, 0.2 mmol SnI₂;
8 CsSn_{0.3}Pb_{0.7}I₃ QDs: 0.037 mmol Cs₂CO₃, 0.2 mmol PbI₂, 0.25 mmol SnI₂) were mixed with 10
9 mL of ODE, 0.5 mL of OA, 0.5 mL of OAM and 0.5 mL of TOP in a 50-mL three-neck flask.
10 OA, OAM and TOP were utilized to limit the particle size and to passivate the surface defects
11 of tin-doped PQDs. Then, the mixture was stirred and heated at 100 °C for 30 minutes under
12 nitrogen atmosphere to obtain a red solution, including nano-sized and micron-sized tin-doped
13 perovskites. To extract and purify tin-doped PQDs, 10 mL of MeOAc was added into the red
14 solution, followed by centrifuging at 7000 rpm for 5 minutes. The supernatant was discarded,
15 and the brown black precipitate was dispersed in 5 mL of hexane. Finally, the brown black
16 solution was centrifuged at 3000 rpm for 5 minutes, and the red supernatant contained only the
17 tin-doped PQDs.

18

19 **Device fabrication**

20 Fluorine-doped SnO₂ (FTO) glasses were washed with water, acetone, isopropanol and ethanol
21 in sequence for 30 minutes each in an ultrasonic cleaner. After that, the FTO glasses were treated
22 by ultraviolet (UV) for 20 minutes to remove residual organic solvents. The compact TiO₂ (c-

1 TiO₂) layer was fabricated on the FTO layer by spin-coating a solution of acetylacetonate (0.1
2 mL) diluted in ethanol (1.9 mL) with the speed of 4000 rpm for 30 s. Then the glasses were
3 annealed at 150 °C for 5 minutes and at 500 °C for 30 minutes. Subsequently, the mesoporous
4 TiO₂ (m-TiO₂) layer was obtained by spin-coating a solution of TiO₂ paste diluted in ethanol
5 onto the c-TiO₂ layer at 3500 rpm for 20 s, and annealed at 500 °C for 30 minutes. The annealing
6 process at 500 °C is to obtain TiO₂ layers with improved electron transport performance. Next,
7 to prepare the MAPbI₃ precursor solution, PbI₂ (0.5 mmol) and MAI (0.5 mmol) were mixed
8 with DMF (300 mg) and DMSO (39 mg). Afterwards, the MAPbI₃ layer was fabricated by spin-
9 coating the MAPbI₃ precursor solution (35 μL) onto the m-TiO₂ layer, with the speed of 1000
10 rpm for 10 s and 4000 rpm for 20 s, followed by heating at 100 °C for 10 minutes. After that,
11 tin-doped PQDs dispersed in toluene (10 mg mL⁻¹) were spin-coated onto the perovskite layer
12 at 4000 rpm for 30 s and annealed at 90 °C for 5 minutes to remove the residual toluene. Finally,
13 the carbon electrode paste was screen-printed on the device and annealed at 100 °C for 10
14 minutes.

15

16 **Characterization**

17 Transmission electron microscope (TEM) images, selected area electron diffraction (SAED)
18 views and energy dispersive X-ray spectroscopy (EDS) analyses of tin-doped PQDs were
19 obtained by a field emission high-resolution transmission electron microscope (JEM-2100F,
20 JEOL, Japan) at an accelerating voltage of 200 kV. The valence band (VB) edges of different
21 materials were acquired from an X-ray photoelectron spectrometer (ESCALAB 250Xi, Thermo
22 Fisher Scientific, US). Absorption and steady-state photoluminescence (PL) characteristics

1 were collected via an UV-visible spectrophotometer (UV-3600, Shimadzu, Japan) and a
2 fluorescence spectrometer (RF-6000, Shimadzu, Japan), respectively. The cross-section image
3 of the PSC and the surface morphologies of perovskite films were obtained by a scanning
4 electron microscope (Zeiss Ultra Plus, Zeiss, Germany). Curves of photocurrent density versus
5 on voltage ($J-V$) were measured by a sourcemeter (2400, Keithley, US) with a sunlight simulator
6 (Oriel Sol3A, Newport, US), under AM 1.5G simulated illumination (100 mW cm^{-2}).
7 Monochromatic incident photon-to-electron conversion efficiency (IPCE) spectra and
8 electrochemical impedance spectroscopies (EIS) were obtained from an electrochemical
9 workstation (Zahner, Kronach, Germany). Finally, X-ray diffraction (XRD) patterns of
10 perovskite films were acquired from an X-ray diffractometer (Empyrean, PANalytical,
11 Netherlands).

12

13 **Results and Discussion**

14 Three kinds of tin-doped PQDs were studied in this work, including $\text{CsSn}_{0.1}\text{Pb}_{0.9}\text{I}_3$ QDs,
15 $\text{CsSn}_{0.2}\text{Pb}_{0.8}\text{I}_3$ QDs and $\text{CsSn}_{0.3}\text{Pb}_{0.7}\text{I}_3$ QDs. The actual atomic ratio of Sn in these PQDs were
16 estimated to be 13.03%, 22.12% and 32.57%, respectively (shown in Fig. S1 and Table S1-S3).
17 As shown in Fig. 1, blue-shifts of the steady-state PL peak (673 nm, 669 nm and 656 nm in
18 turn) and the edge of Tauc plot (1.79 eV, 1.80 eV and 1.81 eV in turn) were observed with the
19 increase of Sn doping. The bandgap is known to increase with the decrease of the unit cell
20 volume [19]. Therefore, more Sn^{2+} substitution would further intensify the lattice contraction,
21 which led to the increased bandgap width, consistent with the reported research [28].

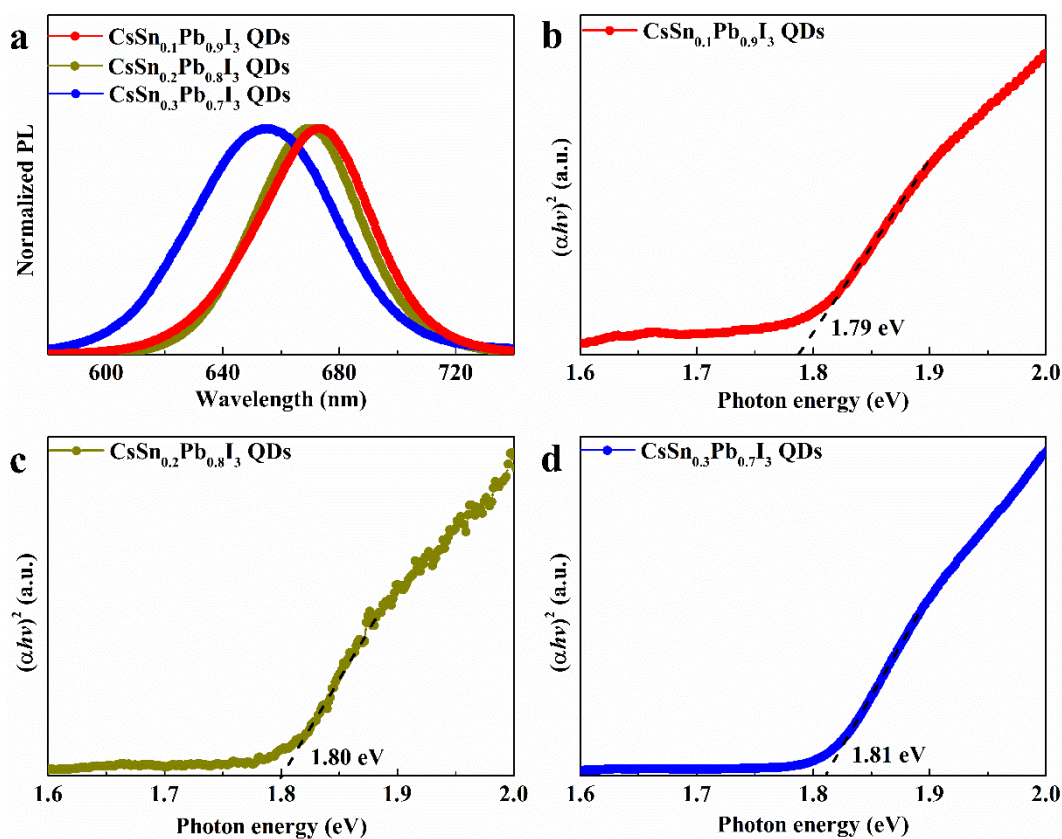
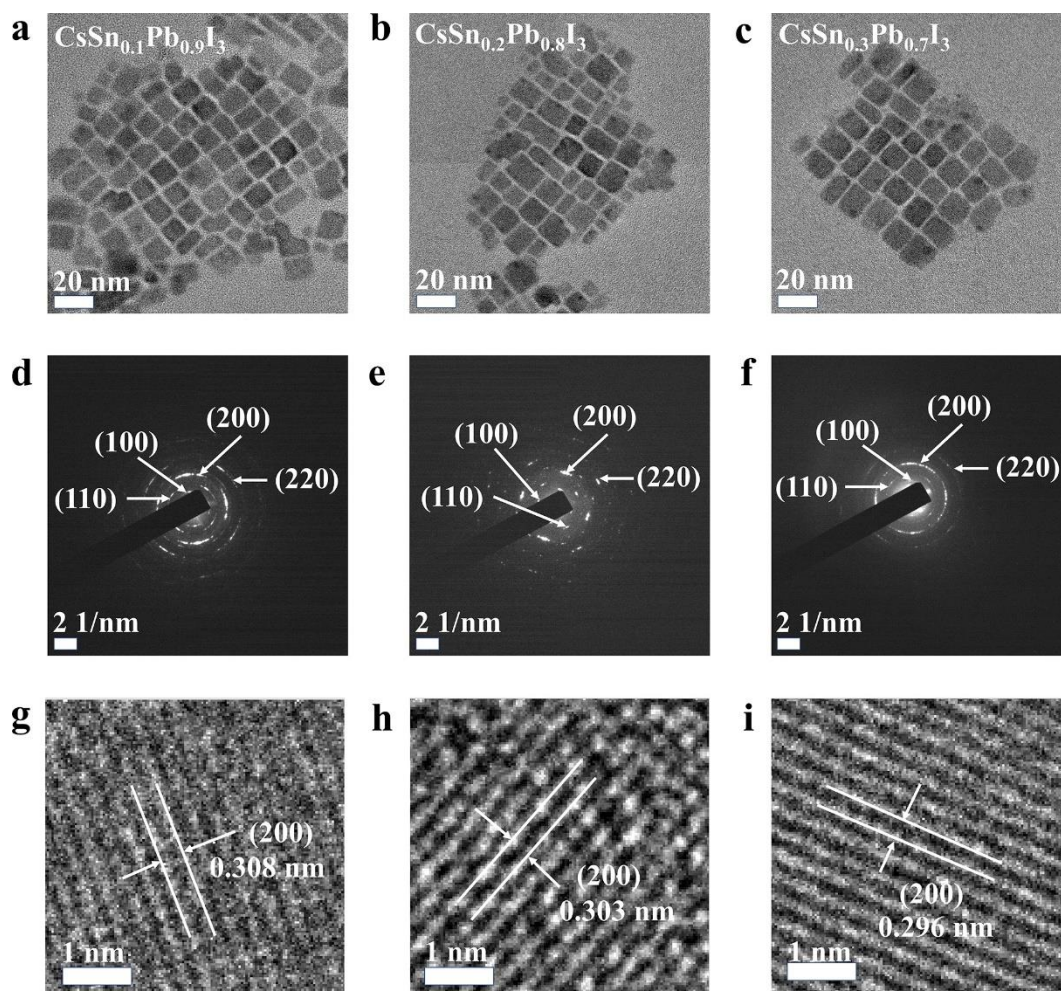


Fig. 1 a Normalized PL spectra and **b-d** Tauc plots of different tin-doped PQDs

The TEM images of these tin-doped PQDs are exhibited in Fig. 2a-c. These tin-doped PQDs were all square, consistent with the theoretical lattice structure of cubic phase. Besides, all these PQDs showed an average size of about 15 nm with good homogeneity. The size of the three kinds of quantum dots was not much different. That was because the size of PQDs was mainly determined by the reaction temperature, and the synthesis temperature of these three kinds of PQDs was kept at 100°C. Besides, corresponding SAED measurements are shown in Fig. 2d-f. By comparing the interplanar spacing values of different diffraction rings with corresponding standard values (CsPbI₃ in cubic phase, ICSD, 181288), some crystal planes including (100), (110), (200) and (220) could be identified, which also indicated that these tin-doped PQDs were mostly composed of cubic nanocrystals (NCs) [20]. Moreover, enlarged

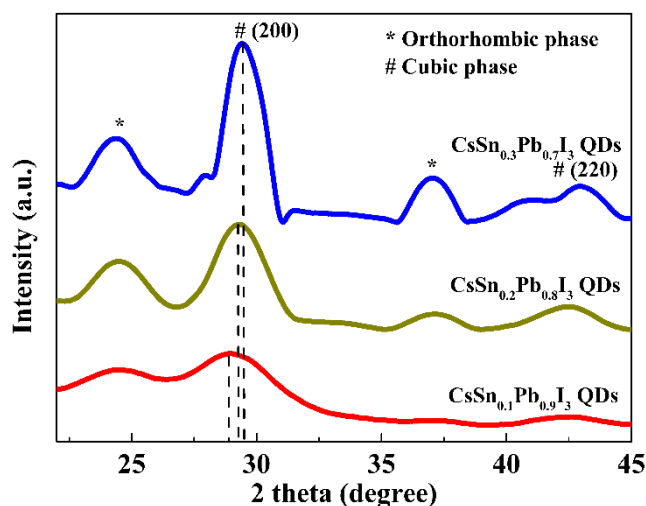
1 TEM images shown in Fig. 2g-i are utilized to further study the crystal plane characteristics.
 2 The interplanar distances of (200) plane of these tin-doped PQDs were determined to be 0.308
 3 nm, 0.303 nm and 0.296 nm in turn, which could demonstrate that increasing substitution of
 4 Pb^{2+} by Sn^{2+} further led to the lattice shrinkage, in accordance with their optical characteristics
 5 mentioned above.



6
 7 **Fig. 2** a-c TEM images, d-f SAED patterns and g-i enlarged TEM images of $\text{CsSn}_{0.1}\text{Pb}_{0.9}\text{I}_3$ QDs,
 8 $\text{CsSn}_{0.2}\text{Pb}_{0.8}\text{I}_3$ QDs and $\text{CsSn}_{0.3}\text{Pb}_{0.7}\text{I}_3$ QDs.

9
 10 To further study the lattice structures of these tin-doped PQDs, we performed XRD
 11 measurements, shown in Fig. 3. According to the standard XRD data of CsPbI_3 in orthorhombic

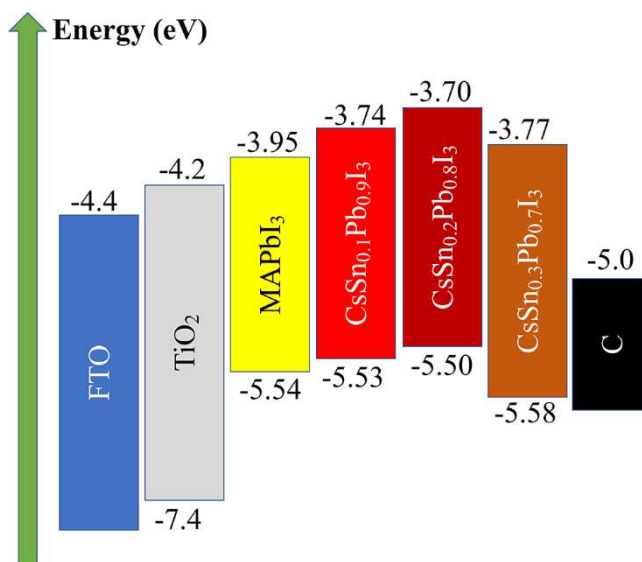
1 and cubic phase [20, 29], the diffraction peaks of these tin-doped PQDs associated with
 2 orthorhombic and cubic phase were marked with “*” and “#”, respectively. As the amount of
 3 Sn doping in PQDs increased, the diffraction angle corresponding to (200) plane slightly
 4 increased, showing that the interplanar distance of (200) plane was reduced, in line with the
 5 analysis above. Meanwhile, the intensities of orthorhombic phase diffraction peaks also showed
 6 increasing trends, which indicated that the phase transition process in the PQDs increased. That
 7 was because the increase in the amount of Sn doping would intensify the oxidation reaction of
 8 the PQDs in the air, resulting in more Sn vacancies, which may make Pb refill these vacancies
 9 to form an unstable perovskite structure.



10
 11 **Fig. 3** XRD patterns of different tin-doped PQDs

12
 13 Optimized band alignment is crucial for enhancing the extraction of photogenerated
 14 carriers and suppressing charge recombination [30-33]. Fig. 4 shows the band structures of
 15 various materials including FTO, TiO₂, MAPbI₃, CsSn_{0.1}Pb_{0.9}I₃ QDs, CsSn_{0.2}Pb_{0.8}I₃ QDs,
 16 CsSn_{0.3}Pb_{0.7}I₃ QDs and carbon. Corresponding UPS and Tauc plots are shown in Fig. S2. It is
 17 clear that the valence band (VB) edge of CsSn_{0.1}Pb_{0.9}I₃ QDs (-5.53 eV) and CsSn_{0.2}Pb_{0.8}I₃ QDs

1 (-5.50 eV) was higher than that of MAPbI₃ (-5.54 eV), satisfying the band alignment
 2 requirement. It was able to eliminate the large Schottky barrier formed by the MAPbI₃/carbon
 3 junction, thus enhancing the hole extraction ability (discussed later) [31]. Furthermore, the
 4 higher conduction band (CB) edges of these tin-doped PQDs were expected to hinder the flow
 5 of electrons from MAPbI₃ to the carbon electrode. However, the VB edge of CsSn_{0.3}Pb_{0.7}I₃ QDs
 6 was lower than that of MAPbI₃, which would block the hole injection, leading to more charge
 7 recombination at the interface between MAPbI₃ and the PQDs.



8
 9 **Fig. 4** Band structures of different materials in PSCs

10
 11 Moreover, the VB edge originates from the interactions between Pb and I orbitals, which
 12 is also determined by the Sn doping amount. On the one hand, the substitution of Pb²⁺ by Sn²⁺
 13 will shrink the lattice structure, leading to shorter Pb-I bonds and stronger interactions between
 14 Pb and I orbitals, so that the VB tends to shift to a higher energy [19]. On the other hand, more
 15 lattice distortions (transformation from cubic NCs to orthorhombic NCs) will be introduced
 16 into the PQDs with the excessive Sn²⁺ substitution, resulting in expanded volume of [PbI₆]

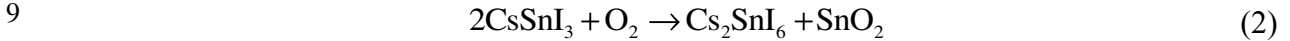
1 octahedra and weaker Pb-I interactions, thus moving the VB to a lower energy position [21].

2 As a result, a reasonable Sn doping content is the key to obtaining an appropriate band structure.

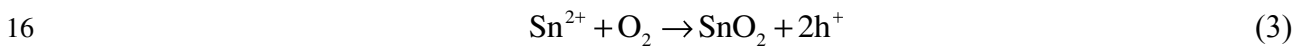
3 Unlike ordinary lead-based PQDs, tin-doped PQDs will partially undergo oxidation in air
4 due to the presence of Sn^{2+} , described by



6 $\text{CsSn}_x\text{Pb}_{1-x}\text{I}_3$ can be assumed to be the combination of CsSnI_3 and CsPbI_3 with a certain molar
7 ratio. Among the compounds, only CsSnI_3 participates in the oxidation reaction. And then, this
8 process can be simplified to



10 In reaction (2), the transformation from CsSnI_3 to Cs_2SnI_6 is regarded as breaking the
11 connections between $[\text{SnI}_6]$ octahedra. The reason is that CsSnI_3 is formed by corner sharing
12 $[\text{SnI}_6]$ octahedra while Cs_2SnI_6 is made up of isolated $[\text{SnI}_6]$ octahedra [22]. Therefore, this half
13 of Sn atoms do not leave the perovskite lattice. However, the other half of Sn atoms are oxidized
14 to SnO_2 , leaving a lot of Sn vacancies in the lattice, which will accept electrons (or supply holes)
15 and act as p-type dopants. It can be described by the equation (3) below

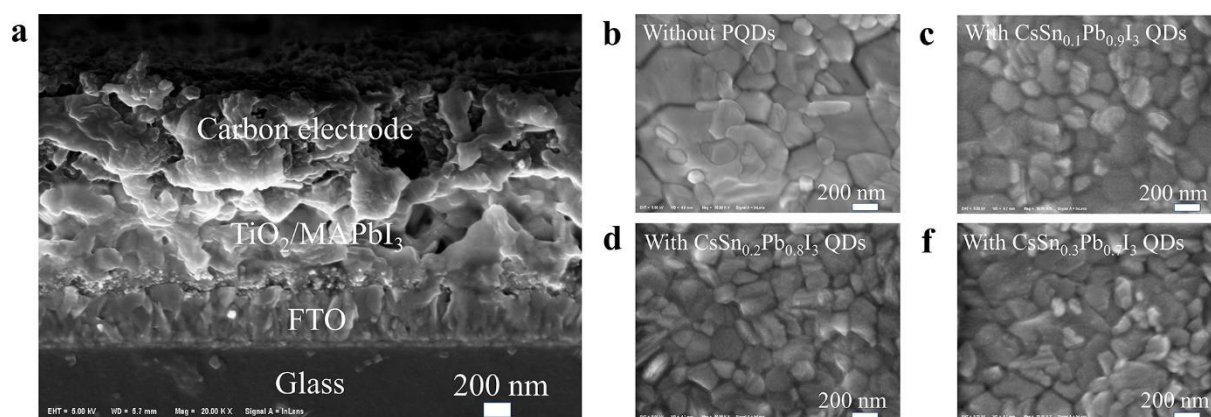


17 That is the reason for the self-p-type doping effects of tin-doped PQDs. Accordingly, under the
18 premise that the lattice structure of tin-doped PQDs can be stabilized, the more Sn^{2+} doping,
19 the higher acceptor concentration of the PQDs.

20 The cross-sectional image of the PSC is shown in Fig. 5a. The widths of FTO layer and
21 $\text{TiO}_2/\text{MAPbI}_3$ composite layer were about 400 nm and 800 nm, respectively. Because of the
22 low concentration of the PQD solution (10 mg mL^{-1}), it was hard to observe a PQD layer that

1 could be distinguished from the underlying MAPbI₃ film. Besides, as shown in Fig. 5b-f, there
2 were many small-sized white PbI₂ particles on the original perovskite film, which was caused
3 by the partial decomposition of the perovskite in the air. After adding tin-doped PQDs, the
4 number of white particles decreased, and the perovskite films exhibited slightly better grain
5 uniformity and compactness than the control sample. However, the morphology difference
6 between the various perovskite films was still not obvious. In order to further distinguish their
7 surface characteristics, we performed grazing incidence XRD (GIXRD) patterns of perovskite
8 films with different tin-doped PQDs, exhibited in Fig. 6. The diffraction peak at about 12.7° is
9 associated with PbI₂ [34]. After the modification of tin-doped PQDs, the intensity of PbI₂-peak
10 was weakened while the intensity of the diffraction peak corresponding to (110) plane of the
11 perovskite increased, indicating that the decomposition process of the perovskite film was
12 suppressed.

13



15 **Fig. 5 a** Cross-sectional image of the PSC. **b-f** Perovskite films without and with tin-doped
16 PQDs.

17

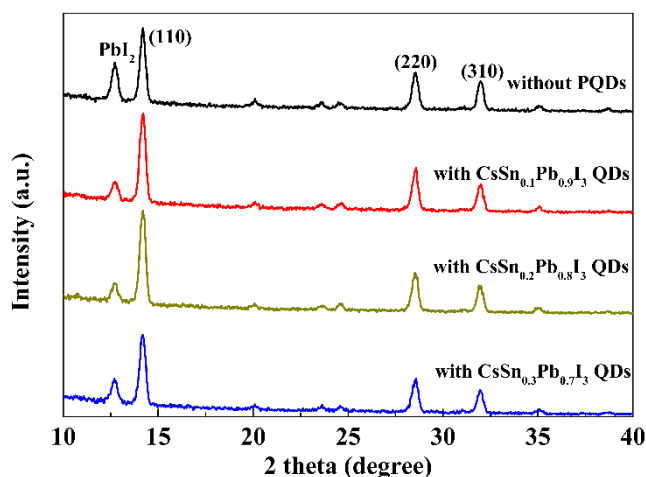


Fig. 6 GIXRD patterns of different perovskite films

1
2
3
4
5
6
7
8
9
10
11
12
13
14
15
16
17

The curves of photocurrent density versus on voltage (J - V) of different PSCs are displayed in Fig. 7a, and photovoltaic parameters including short circuit current density (J_{sc}), open circuit voltage (V_{oc}), fill factor (FF) and PCE are shown in Table 1. The values of J_{sc} , V_{oc} , FF, and PCE of the PSC without modification by tin-doped PQDs were 22.69 mA cm⁻², 0.99 V, 56.78% and 12.80%, respectively. For the CsSn_{0.1}Pb_{0.9}I₃ QDs-added PSC, various parameters were improved. However, the improvement was not optimal, which might ascribe to the relatively low Sn doping of the PQDs. In contrast, with the incorporation of CsSn_{0.2}Pb_{0.8}I₃ QDs, a J_{sc} of 23.30 mA cm⁻², a V_{oc} of 1.05 V, a FF of 57.90% and a PCE of 14.22% could be obtained. The significant increase in each parameter indicated the reduction of non-radiative recombination and the effective extraction of photogenerated holes. Besides, as shown in Fig. S3, PCE values for 90% of CsSn_{0.2}Pb_{0.8}I₃ QDs-added PSCs surpassed 13%, showing good repeatability. But for the PSC modified by CsSn_{0.3}Pb_{0.7}I₃ QDs, the values of J_{sc} and FF seriously dropped to 16.82 mA cm⁻² and 47.40%, respectively. The lower VB edge of the PQDs would hinder the hole transfer from the MAPbI₃ film to the carbon electrode. Furthermore, when the Sn content of

1 PQDs was too high, more Sn vacancies would be introduced, which would not only provide
2 more free holes, but also result in more phase transformation products with large bandgap
3 widths [29, 35-37], and thus seriously impeding the transport process of photogenerated carriers.

4 As described in Fig. 7b, the IPCE spectra in a wavelength range from 350 nm to 800 nm
5 increased in the order of CsSn_{0.3}Pb_{0.7}I₃ QDs-added device < control device < CsSn_{0.1}Pb_{0.9}I₃
6 QDs-added device < CsSn_{0.2}Pb_{0.8}I₃ QDs-added device, in agreement with the corresponding
7 trend of J_{sc} acquired from the $J-V$ curves. It is clear that the difference of these IPCE curves
8 was mainly reflected in the wavelength range from 550 nm to 800 nm. Tin-doped PQDs added
9 onto the perovskite film would significantly affect the built-in electric field near the back
10 surface of the perovskite (analyzed in detail later). At the same time, these long-wavelength
11 lights were mainly absorbed by the perovskite near the back surface due to their low energy.
12 After these photons were converted into carriers, their transport properties would be more easily
13 changed by the above-mentioned built-in electric field than those photogenerated carriers of
14 short-wavelength lights.

15 In addition, EIS measurements, in a frequency range from 4 MHz to 0.2 MHz at a bias of
16 0.8 V under simulated AM 1.5G radiation, were performed to analyze the charge transport
17 resistance (R_{CT}) and the barrier capacitance (C_T) near the carbon electrode, described in Fig. 7c.
18 Corresponding EIS parameters are also shown in Table 1. With the addition of CsSn_{0.2}Pb_{0.8}I₃
19 QDs, the R_{CT} value was reduced, which meant the promoted hole extraction and the decreased
20 energy loss on the back surface of MAPbI₃. Furthermore, compared with the pristine and the
21 CsSn_{0.1}Pb_{0.9}I₃ QDs-added PSCs, the value of C_T increased, so that a shorter depletion width
22 near the back surface of MAPbI₃ (W_D) could be deduced based on the following formulas,

1 suggesting facilitated hole transfer.

$$2 \quad C_T = \frac{C_1 C_2}{C_1 + C_2} \quad (4)$$

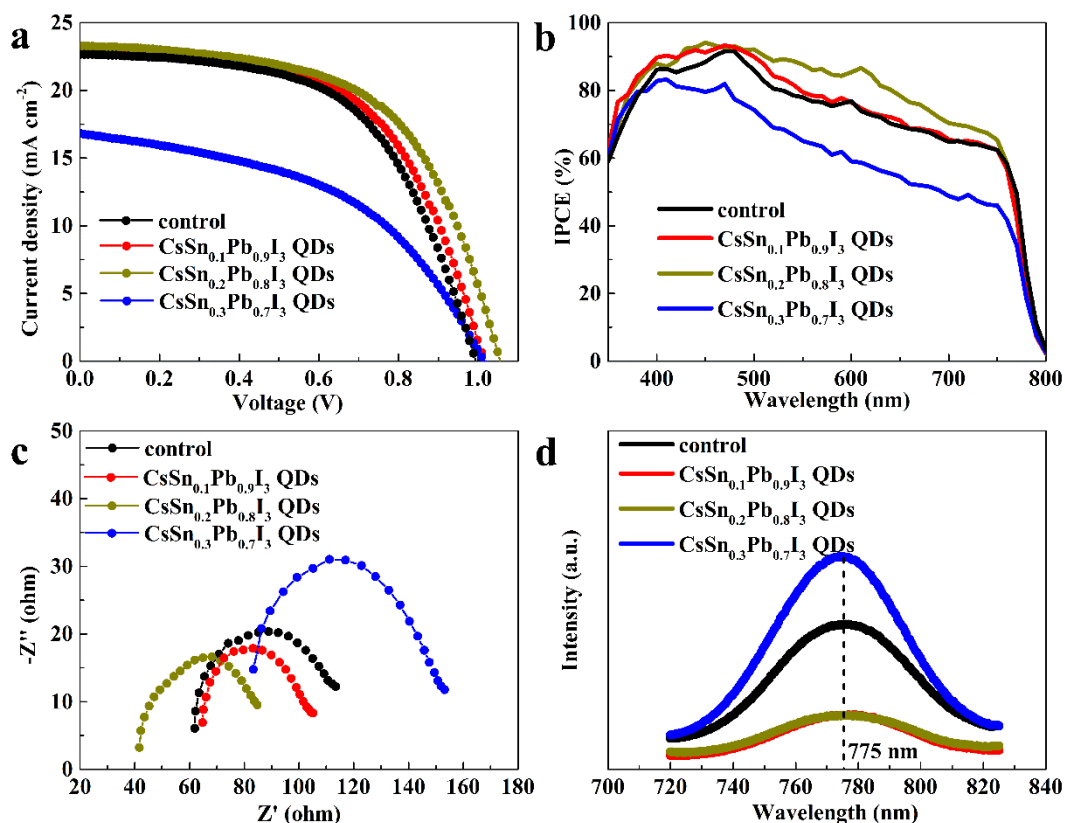
$$3 \quad C_1 = \frac{\epsilon_{\text{MAPbI}_3} A}{W_D} \quad (5)$$

$$4 \quad C_2 = \frac{\epsilon_{\text{QD}} A}{d_{\text{QD}}} \quad (6)$$

5 where A is the active area and d_{QD} is the width of the PQD layer. It is worth noting that the
6 contact between MAPbI₃ and the PQDs would form a hole depletion region in MAPbI₃. Then,
7 the contact between the PQDs and the carbon electrode would generate a Schottky barrier,
8 which led to a hole depletion region in the PQD layer. Both the depletion regions in MAPbI₃
9 and the PQDs contributed to the barrier capacitance value. For the PSC in the presence of
10 CsSn_{0.3}Pb_{0.7}I₃ QDs, the lower VB edge of the PQDs allowed more holes to migrate from the
11 PQD layer to the MAPbI₃ film. These holes gradually moved away from the MAPbI₃/PQDs
12 interface under the isotype heterojunction electric field, thereby increasing the W_D . This might
13 be the reason why the C_T value of CsSn_{0.3}Pb_{0.7}I₃ QDs-added device was low.

14 To get insight on the carrier transfer process, the steady-state PL spectra for the pure
15 MAPbI₃ film and MAPbI₃ films covered by different tin-doped PQDs were measured. As shown
16 in Fig. 7d, the PL peak intensity at about 775 nm was obviously decreased after the
17 incorporation of CsSn_{0.1}Pb_{0.9}I₃ QDs or CsSn_{0.2}Pb_{0.8}I₃ QDs. There were two explanations for the
18 weakening of PL intensity: first, the PQDs cause additional non-radiative pathways to capture
19 photogenerated carriers; second, the higher VB edges of PQDs allow more photogenerated
20 holes to migrate to the PQD layer, thus the number of carriers participating in direct
21 recombination is reduced. However, after adding CsSn_{0.3}Pb_{0.7}I₃ QDs with more orthorhombic

1 by-products and lower VB edge, the PL intensity increased, which showed that more carriers
 2 were limited in the perovskite film without being trapped by defects. Therefore, the PL quench
 3 of the perovskite film with $\text{CsSn}_{0.1}\text{Pb}_{0.9}\text{I}_3$ QDs or $\text{CsSn}_{0.2}\text{Pb}_{0.8}\text{I}_3$ QDs was caused by the
 4 optimized band alignment promoting the hole extraction, instead of interfacial trap-assisted
 5 recombination.



6
 7 **Fig. 7** a $J-V$ curves, b IPCE spectra and c EIS measurements of different PSCs. d PL spectra of
 8 perovskite films with and without tin-doped PQDs.

9
 10
 11
 12
 13

1 **Table 1** Photovoltaic parameters of different PSCs

Device	V_{oc} (V)	J_{sc} (mA cm ⁻²)	FF (%)	PCE (%)	R_{CT} (Ω)	C_T (nF)
Control	0.99	22.69	56.78	12.80	56.5	35.5
With CsSn _{0.1} Pb _{0.9} I ₃ QDs	1.01	22.85	57.81	13.38	47.0	32.9
With CsSn _{0.2} Pb _{0.8} I ₃ QDs	1.05	23.30	57.90	14.22	43.0	44.7
With CsSn _{0.3} Pb _{0.7} I ₃ QDs	1.01	16.82	47.40	8.07	81.4	16.3

2

3 In order to further understand the effects of tin-doped PQDs on the hole transport in
4 MAPbI₃ films, a one-dimensional MAPbI₃/tin-doped PQDs heterojunction model was
5 constructed, shown in Fig. 8a. To simplify the analysis, this structure was regarded as a mutant
6 isotype heterojunction, and MAPbI₃ and tin-doped PQDs were determined to be p-type
7 semiconductors. Theoretically, MAPbI₃ is a kind of intrinsic semiconductor with low doping
8 amount, but in the carbon-based perovskite PSCs with no HTLs, the perovskite layer needs to
9 undergo p-type doping treatment. A small amount of DMSO were added in the precursor of
10 perovskite to form a complex with PbI₂, so that there was a small amount of Pb vacancy in the
11 perovskite, which made the perovskite become a p-type semiconductor. Moreover, Laban and
12 Etgar utilized Mott-Schottky analysis to find that the acceptor concentration of MAPbI₃ was
13 $2.14 \times 10^{17} \text{ cm}^{-3}$, belonging to the doping level of p-type semiconductor [38]. The contact of two
14 semiconductors with different Fermi levels would form an electric field from the one with a
15 high Fermi level to the another with a low Fermi level. Consequently, the p-p isotype
16 heterojunction energy-band diagram under the equilibrium condition could be obtained, shown
17 in Fig. 8b. According to the Poisson's equation, the field continuity condition and the depletion

1 approximation [39], barrier distributions of the isotype heterojunction were expressed by the
 2 following equations

$$3 \quad \exp\left(\frac{qV_{D_QD}}{k_B T}\right) - \frac{qV_{D_QD}}{k_B T} - 1 = \frac{\epsilon_{MAPbI_3} N_{A_MAPbI_3}}{\epsilon_{QD} N_{A_QD}} \frac{qV_{D_MAPbI_3}}{k_B T} \quad (7)$$

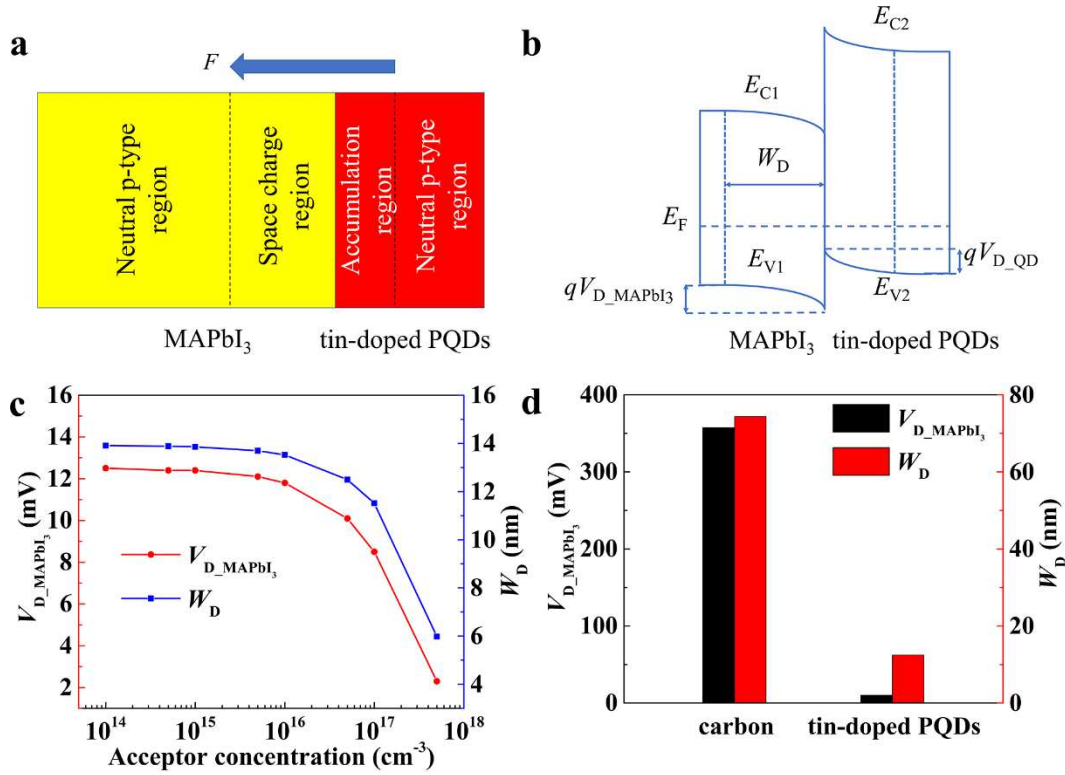
$$4 \quad qV_{D_MAPbI_3} + qV_{D_QD} = E_{Fermi_QD} - E_{Fermi_MAPbI_3} \quad (8)$$

$$5 \quad E_{Fermi}^p = \frac{1}{2} E_{CB} + E_{VB} - \frac{1}{2} k_B T \ln\left(\frac{N_C}{N_V}\right) - k_B T \ln\left(\frac{N_a}{n_i}\right) \quad (9)$$

$$6 \quad W_D = \sqrt{\frac{2\epsilon_{MAPbI_3} V_{D_MAPbI_3}}{qN_{A_MAPbI_3}}} \quad (10)$$

7 where q is the elementary charge, ϵ_{QD} and N_{A_QD} are the dielectric coefficient and the acceptor
 8 concentration for tin-doped PQDs, respectively. $V_{D_MAPbI_3}$ and V_{D_QD} are the potential difference
 9 in MAPbI₃ and tin-doped PQDs in turn. $E_{Fermi_MAPbI_3}$ and E_{Fermi_QD} stand for the Fermi levels of
 10 MAPbI₃ and tin-doped PQDs, respectively. k_B is the Boltzmann constant and T is the room
 11 temperature. N_C and N_V are the effective density of states of electrons in conduction band and
 12 the effective density of states of holes in valence band, respectively. N_a is the acceptor
 13 concentration, n_i is the intrinsic carrier concentration and W_D is the depletion width in MAPbI₃.
 14 The simulation results are exhibited in Fig. 8c. As the acceptor concentration of tin-doped PQDs
 15 increased, both $V_{D_MAPbI_3}$ and W_D showed downward trends, indicating that the hole transfer
 16 process in the MAPbI₃ film was gradually facilitated. Besides, less electrons would be drifted
 17 to the interface between MAPbI₃ and the PQD layer to recombine with holes. On the contrary,
 18 the direct contact between MAPbI₃ and the carbon electrode would generate a large Schottky
 19 barrier in MAPbI₃, resulting in higher values of $V_{D_MAPbI_3}$ and W_D , shown in Fig. 8d. In one
 20 word, MAPbI₃ films modified by tin-doped PQDs with higher acceptor concentrations would
 21 be provided with much enhanced hole transport performance. This simulation result explained

1 why the photovoltaic performance of the $\text{CsSn}_{0.2}\text{Pb}_{0.8}\text{I}_3$ QDs-added PSC was better than the
 2 pristine and the $\text{CsSn}_{0.1}\text{Pb}_{0.9}\text{I}_3$ QDs-added device.



3
 4 **Fig. 8 a** The one-dimensional $\text{MAPbI}_3/\text{PQDs}$ heterojunction model. **b** Corresponding energy-
 5 band diagram under the equilibrium condition. **c** and **d** Simulation results for $\text{MAPbI}_3/\text{PQDs}$
 6 and $\text{MAPbI}_3/\text{carbon}$ heterojunctions.

7

8 Conclusions

9 In summary, tin-doped PQDs were added between MAPbI_3 and the carbon electrode for
 10 enhanced PSC performance, due to their flexible energy levels and self-p-type doping effects.

11 Especially, with the incorporation of $\text{CsSn}_{0.2}\text{Pb}_{0.8}\text{I}_3$ QDs, the PCE value could be improved
 12 from 12.80% to 14.22%, in comparison to the pristine device. It was attributed to the band
 13 alignment and the appropriate Sn^{2+} doping content of the PQDs facilitating the hole extraction.

14 This work is prospected to provide a direction for the interface optimization of carbon-based

1 PSCs based on PQDs.

2

3 **Abbreviations**

4 PSCs: perovskite solar cells; PQDs: perovskite quantum dots; HTLs: hole-transporting layers;

5 PCE: power conversion efficiency; ODE: 1-octadecene; OA: oleic acid; OAM: oleylamine

6 MeOAc: methyl acetate; TOP: trioctylphosphine; MAI: methylammonium; DMSO:

7 dimethylsulfoxide; DMF: N,N-dimethylformamide; FTO: fluorine-doped SnO₂; c-TiO₂:

8 compact TiO₂; m-TiO₂: mesoporous TiO₂; TEM: transmission electron microscope; SAED:

9 selected area electron diffraction; EDS: energy dispersive X-ray spectroscopy; VB: valence

10 band; PL: photoluminescence; IPCE: incident photon-to-electron conversion; EIS:

11 electrochemical impedance spectroscopy; XRD: X-ray diffraction.

12

13 **Authors' contributions**

14 CZ performed the experiments and drafted the manuscript with the help of ZYH, XHL, RWM.

15 MWC, HFL and YPY helped to revised the manuscript. All authors read and approved the final

16 manuscript.

17

18 **Funding**

19 This work was supported by the National Natural Science Foundation of China (NSFC)

20 (11704293, 11974266) and the Fundamental Research Funds for the Central Universities under

21 Grant WUT (2020IB022).

22

1 **Availability of data and materials**

2 The datasets used and/or analyzed during the current study are available from the corresponding
3 author on reasonable request.

4

5 **Competing interests**

6 The authors declare that they have no competing interests.

7

8 **Acknowledgements**

9 Not applicable

10

11 **References**

- 12 1. Rong YG, Hu Y, Mei AY, Tan HR, Saidaminov MI, Seok SI, McGehee MD, Sargent EH, Han
13 HW. Challenges for commercializing perovskite solar cells. *Science*. 2018;361:eaat8235.
- 14 2. Liao JF, Wu WQ, Jiang Y, Zhong JX, Wang LZ, Kuang DB. Understanding of carrier
15 dynamics, heterojunction merits and device physics: towards designing efficient carrier
16 transport layer-free perovskite solar cells. *Chem Soc Rev*. 2020;49:354-381.
- 17 3. Huang JS, Yuan YB, Shao YC, Yan YF. Understanding the physical properties of hybrid
18 perovskites for photovoltaic applications. *Nat Rev Mater*. 2017;2:17042.
- 19 4. Hwang T, Yun AJ, Kim J, Cho D, Kim S, Hong S, Park B. Electronic traps and their
20 correlations to perovskite solar cell performance via compositional and thermal annealing
21 controls. *ACS Appl Mater Interfaces*. 2019;11:6907-6917.
- 22 5. Zhou R, Yang Z, Xu JZ, Cao GZ. Synergistic combination of semiconductor quantum dots

- 1 and organic-inorganic halide perovskites for hybrid solar cells. *Coord Chem Rev.*
2 2018;374:279-313.
- 3 6. Eperon GE, Habisreutinger SN, Leijtens T, Bruijnaers BJ, Van Franeker JJ, DeQuilettes DW,
4 Pathak S, Sutton RJ, Grancini G, Ginger DS, Janssen RAJ, Petrozza A, Snaith HJ. The
5 importance of moisture in hybrid lead halide perovskite thin film fabrication. *ACS Nano.*
6 2015;9:9380-9393.
- 7 7. Meng FN, Liu AM, Gao LG, Cao JM, Yan YL, Wang N, Fan MQ, Wei GY, Ma TL. Current
8 progress in interfacial engineering of carbon-based perovskite solar cells. *J Mater Chem A.*
9 2019;7:8690-8699.
- 10 8. Chen K, Wu P, Yang WQ, Su R, Luo DY, Yang XY, Tu YG, Zhu R, Gong QH. Low-
11 dimensional perovskite interlayer for highly efficient lead-free formamidinium tin iodide
12 perovskite solar cells. *Nano Energy.* 2018;49:411-418.
- 13 9. Akin S, Altintas Y, Mutlugun E, Sonmezoglu S. Cesium-lead based inorganic perovskite
14 quantum-dots as interfacial layer for highly stable perovskite solar cells with exceeding 21%
15 efficiency. *Nano Energy.* 2019;60:557-566.
- 16 10. Zheng XP, Troughton J, Gasparini N, Lin YB, Wei MY, Hou Y, Liu JK, Song KP, Chen ZL,
17 Yang C, Turedi B, Alsalloum AY, Pan J, Chen J, Zhumekenov AA, Anthopoulos TD, Han
18 Y, Baran D, Mohammed OF, Sargent EH, Bakr OM. Quantum dots supply bulk- and
19 surface-passivation agents for efficient and stable perovskite solar cells. *Joule.* 2019;3:
20 1963-1976.
- 21 11. Chen LC, Tien CH, Tseng ZL, Ruan JH. Enhanced efficiency of MAPbI₃ perovskite solar
22 cells with FAPbX₃ perovskite quantum dots. *Nanomaterials.* 2019;9:121.

- 1 12. Gao YB, Wu YJ, Lu HB, Chen C, Liu Y, Bai X, Yang LL, Yu WW, Dai QL, Zhang Y.
2 CsPbBr₃ perovskite nanoparticles as additive for environmentally stable perovskite solar
3 cells with 20.46% efficiency. *Nano Energy*. 2019;59:517-526.
- 4 13. Cha MY, Da PM, Wang J, Wang WY, Chen ZH, Xiu FX, Zheng GF, Wang ZS. Enhancing
5 perovskite solar cell performance by interface engineering using CH₃NH₃PbBr_{0.9}I_{2.1}
6 quantum dots. *J Am Chem Soc*. 2016;138:8581-8587.
- 7 14. Sidhik S, Esparza D, Martínez-Benítez A, Lopez-Luke T, Carriles R, Mora-Sero I, de la
8 Rosa E. Enhanced photovoltaic performance of mesoscopic perovskite solar cells by
9 controlling the interaction between CH₃NH₃PbI₃ films and CsPbX₃ perovskite nanoparticles.
10 *J Phys Chem C*. 2017;121:4239-4245.
- 11 15. Li B, Zhang YN, Zhang YL, Yin LW. Graded heterojunction engineering for hole-
12 conductor-free perovskite solar cells with high hole extraction efficiency and conductivity.
13 *Adv Mater*. 2017;29:1701221.
- 14 16. Chan CY, Wang YY, Wu GW, Diao EWG. Solvent-extraction crystal growth for highly
15 efficient carbon-based mesoscopic perovskite solar cells free of hole conductors. *J Mater*
16 *Chem A*. 2016;4:3872-3878.
- 17 17. Sheng YS, Mei AY, Liu SA, Duan M, Jiang P, Tian CB, Xiong YL, Rong YG, Han HW, Hu
18 Y. Mixed (5-AVA)_xMA_{1-x}PbI_{3-y}(BF₄)_y perovskites enhance the photovoltaic performance
19 of hole- conductor-free printable mesoscopic solar cells. *J Mater Chem A*. 2018;6:2360-
20 2364.
- 21 18. Xiong YL, Liu Y, Lan K, Mei AY, Sheng YS, Zhao DY, Han HW. Fully printable hole-
22 conductor-free mesoscopic perovskite solar cells based on mesoporous anatase single

- 1 crystals. *New J Chem.* 2018;42:2669-2674.
- 2 19. Van der Stam W, Geuchies JJ, Altantzis T, Van den Bos KHW, Meeldijk JD, Van Aert S,
3 Bals S, Vanmaekelbergh D, De Mello Donega C. Highly emissive divalent-ion-doped
4 colloidal CsPb_{1-x}M_xBr₃ perovskite nanocrystals through cation exchange. *J Am Chem Soc.*
5 2017;139:4087-4097.
- 6 20. Zhang JB, Zhang LW, Cai P, Xue XG, Wang MK, Zhang J, Tu GL. Enhancing stability of
7 red perovskite nanocrystals through copper substitution for efficient light-emitting diodes.
8 *Nano Energy.* 2019;62:434-441.
- 9 21. Vitoreti ABF, Agouram S, de la Fuente MS, Muñoz-Sanjose V, Schiavon MA, Mora-Sero I.
10 Study of the partial substitution of Pb by Sn in Cs-Pb-Sn-Br nanocrystals owing to obtaining
11 stable nanoparticles with excellent optical properties. *J Phys Chem C.* 2018;122:14222-
12 14231.
- 13 22. Gupta S, Cahen D, Hodes G. How SnF₂ impacts the material properties of lead-free tin
14 perovskites. *J Phys Chem C.* 2018;122:13926-13936.
- 15 23. Mosconi E, Umari P, De Angelis F. Electronic and optical properties of mixed Sn-Pb
16 organohalide perovskites: a first principles investigation. *J Mater Chem A.* 2015;3:9208-
17 9215.
- 18 24. Chung I, Song JH, Im J, Androulakis J, Malliakas CD, Li H, Freeman AJ, Kenney JT,
19 Kanatzidis MG. CsSnI₃: Semiconductor or metal? High electrical conductivity and strong
20 near-infrared photoluminescence from a single material. High hole mobility and phase-
21 transitions. *J Am Chem Soc.* 2012;134:8579-8587.
- 22 25 Liu F, Ding C, Zhang YH, Ripolles TS, Kamisaka T, Toyoda T, Hayase S, Minemoto T,

- 1 Yoshino K, Dai SY, Yanagida M, Noguchi H, Shen Q. Colloidal synthesis of air-stable
2 alloyed $\text{CsSn}_{1-x}\text{Pb}_x\text{I}_3$ perovskite nanocrystals for use in solar cells. *J Am Chem Soc.* 2017;
3 139:16708-16719.
- 4 26. Xu HZ, Duan JL, Zhao YY, Jiao ZB, He BL, Tang QW. 9.13%-efficiency and stable
5 inorganic CsPbBr_3 solar cells. Lead-free $\text{CsSnBr}_{3-x}\text{I}_x$ quantum dots promote charge
6 extraction. *J Power Sources.* 2018;399:76-82.
- 7 27. Duan QQ, Ji JY, Hong X, Fu YC, Wang CY, Zhou K, Liu XQ, Yang H, Wang ZY. Design
8 of hole-transport-material free $\text{CH}_3\text{NH}_3\text{PbI}_3/\text{CsSnI}_3$ all-perovskite heterojunction efficient
9 solar cells by device simulation. *Solar Energy.* 2020;201:555-560.
- 10 28. Zhang XL, Cao WY, Wang WG, Xu B, Liu S, Dai HT, Chen SM, Wang K, Sun XW. Efficient
11 light-emitting diodes based on green perovskite nanocrystals with mixed-metal cations.
12 *Nano Energy.* 2016;30:511-516.
- 13 29. Swarnkar A, Marshall AR, Sanhira EM, Chernomordik BD, Moore DT, Christians JA,
14 Chakrabarti T, Luther JM. Quantum dot-induced phase stabilization of a- CsPbI_3 perovskite
15 for high-efficiency photovoltaics. *Science.* 2016;354:92-95.
- 16 30. Minemoto T, Murata M. Impact of work function of back contact of perovskite solar cells
17 without hole transport material analyzed by device simulation. *Curr Appl Phys.* 2014;14:
18 1428-1433.
- 19 31. Tian CB, Mei AY, Zhang SJ, Tian HR, Liu S, Qin F, Xiong YL, Rong YG, Hu Y, Zhou YH,
20 Xie SY, Han HW. Oxygen management in carbon electrode for high-performance printable
21 perovskite solar cells. *Nano Energy.* 2018;53:160-167.
- 22 32. Jeon NJ, Na H, Jung EH, Yang TL, Lee YG, Kim G, Shin HW, Seok SI, Lee J, Seo J. A

- 1 fluorene-terminated hole-transporting material for highly efficient and stable perovskite
2 solar cells. *Nat Energy*. 2018;3:682-689.
- 3 33. Li C, Wang FZ, Xu J, Yao JX, Zhang B, Zhang CF, Xiao M, Dai SY, Li YF, Tan ZA. Efficient
4 perovskite/fullerene planar heterojunction solar cells with enhanced charge extraction and
5 suppressed charge recombination. *Nanoscale*. 2015;7:9771-9778.
- 6 34. Song JX, Bian J, Zheng EQ, Wang XF, Tian WJ, Miyasaka T. Efficient and environmentally
7 stable perovskite solar cells based on ZnO electron collection layer. *Chem Lett*. 2015;44:
8 610-612.
- 9 35. Sanehira EM, Marshall AR, Christians JA, Harvey SP, Ciesielski PN, Wheeler LM, Schulz
10 P, Lin LY, Beard MC, Luther JM. Enhanced mobility CsPbI₃ quantum dot arrays for record-
11 efficiency, high-voltage photovoltaic cells. *Sci Adv*. 2017;3:eaao4204.
- 12 36. Akkerman QA, Park S, Radicchi E, Nunzi F, Mosconi E, De Angelis F, Brescia R, Rastogi
13 P, Prato M, Manna L. Nearly monodisperse insulator Cs₄PbX₆ (X = Cl, Br, I) nanocrystals,
14 their mixed halide compositions, and their transformation into CsPbX₃ nanocrystals. *Nano*
15 *Lett*. 2017;17:1924-1930.
- 16 37. De Weerd C, Lin JH, Gomez L, Fujiwara Y, Suenaga K, Gregorkiewicz T. Hybridization of
17 single nanocrystals of Cs₄PbBr₆ and CsPbBr₃. *J Phys Chem C*. 2017;121:19490-19496.
- 18 38. Laban WA, Etgar L, Depleted hole conductor-free lead halide iodide heterojunction solar
19 cells. *Energy Environ Sci*. 2013;6:3249-3253.
- 20 39. Kumar RC. On the solution of poisson equation for an isotype heterojunction under zero-
21 current condition. *Solid State Electron*. 1968;11:543-551.

Figures

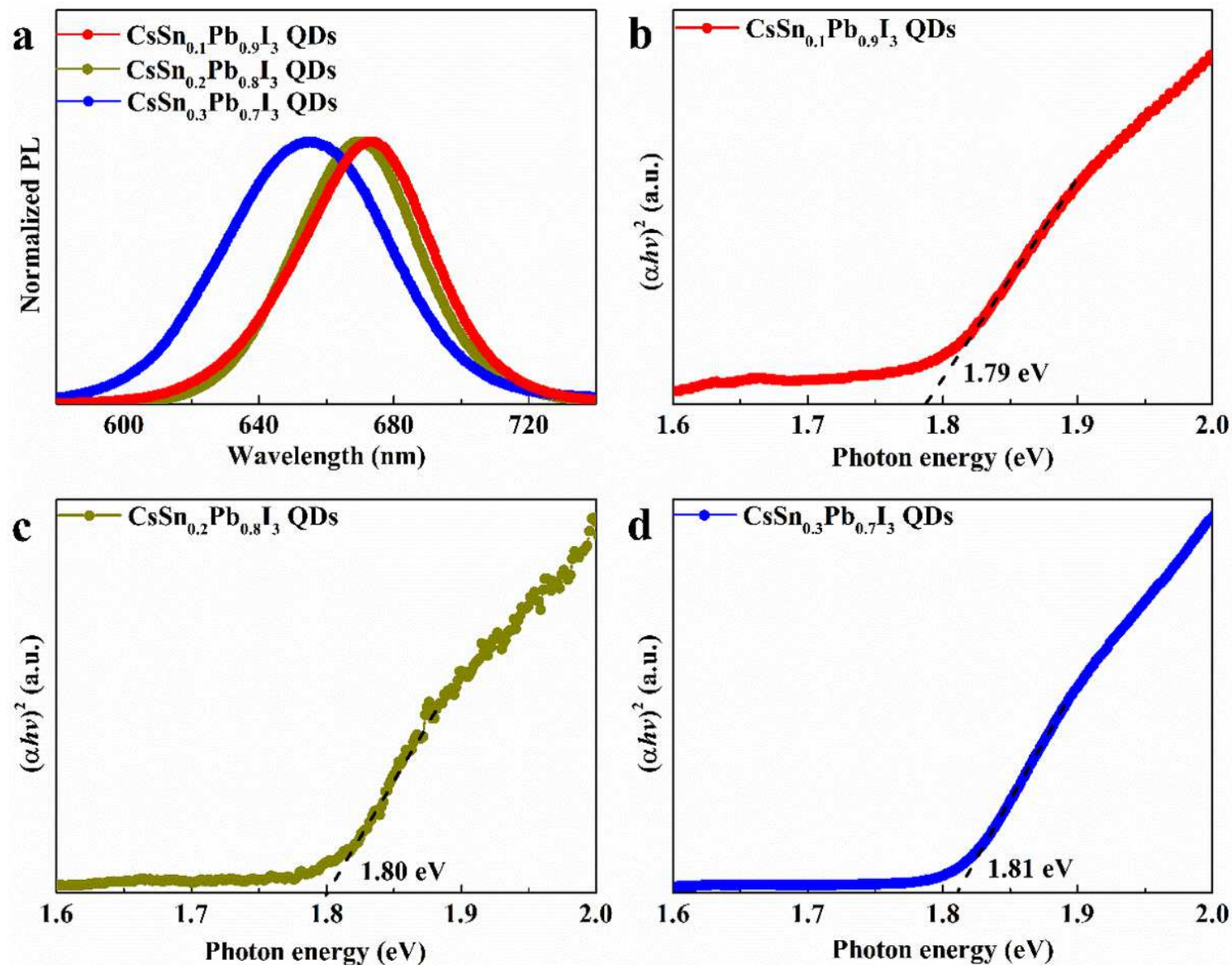


Figure 1

a Normalized PL spectra and b-d Tauc plots of different tin-doped PQDs

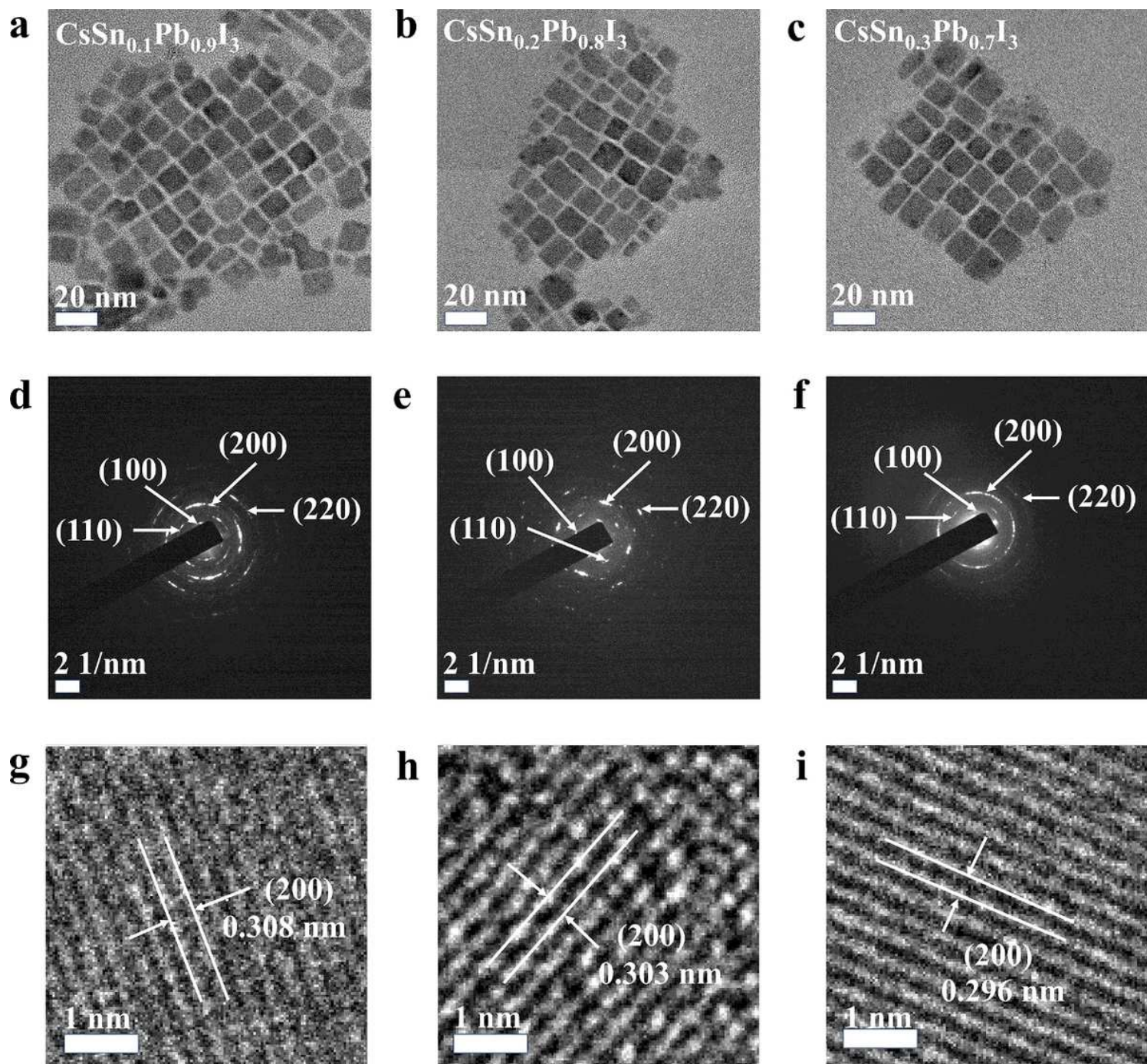


Figure 2

a-c TEM images, d-f SAED patterns and g-i enlarged TEM images of CsSn_{0.1}Pb_{0.9}I₃ QDs, CsSn_{0.2}Pb_{0.8}I₃ QDs and CsSn_{0.3}Pb_{0.7}I₃ QDs.

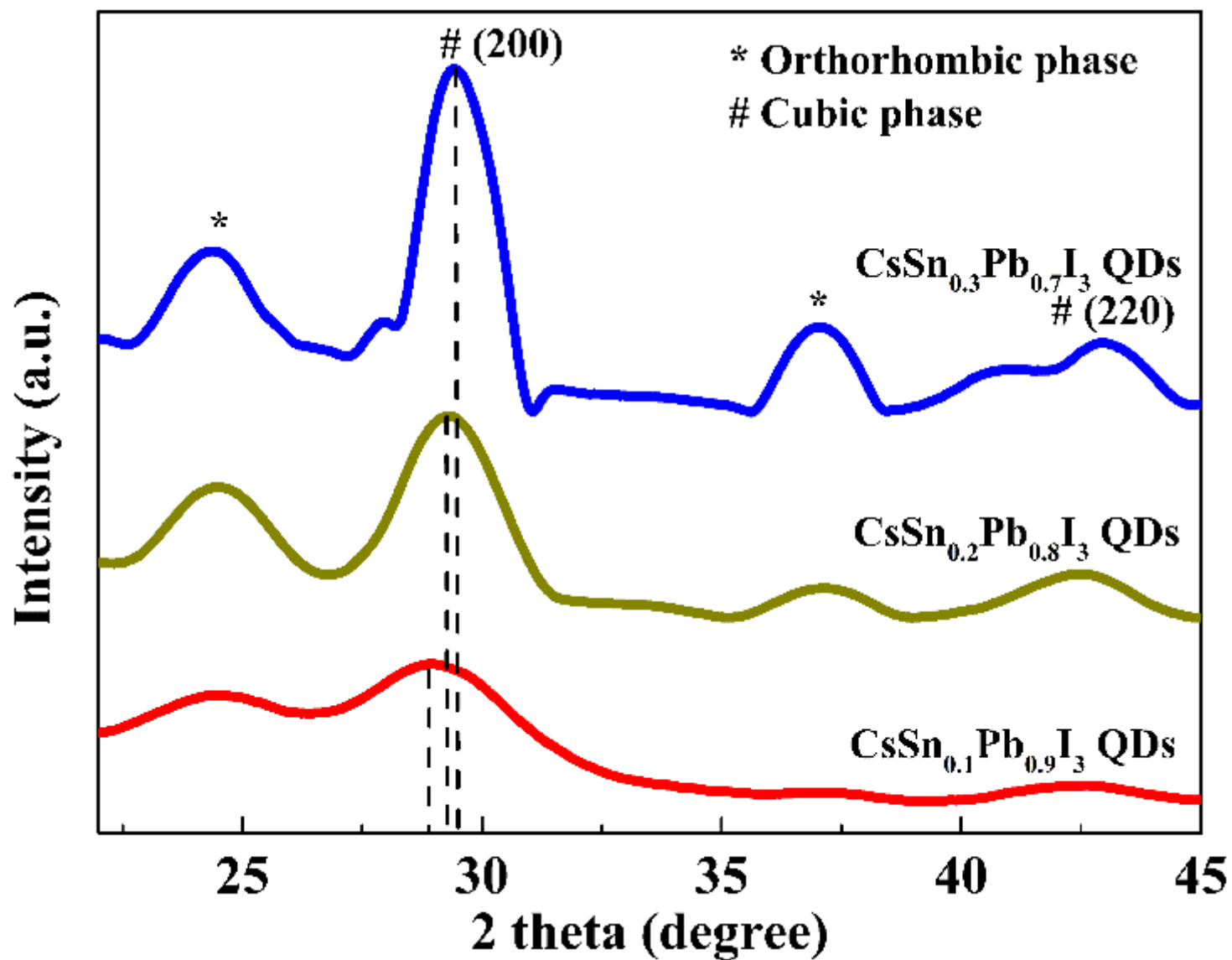


Figure 3

XRD patterns of different tin-doped PQDs

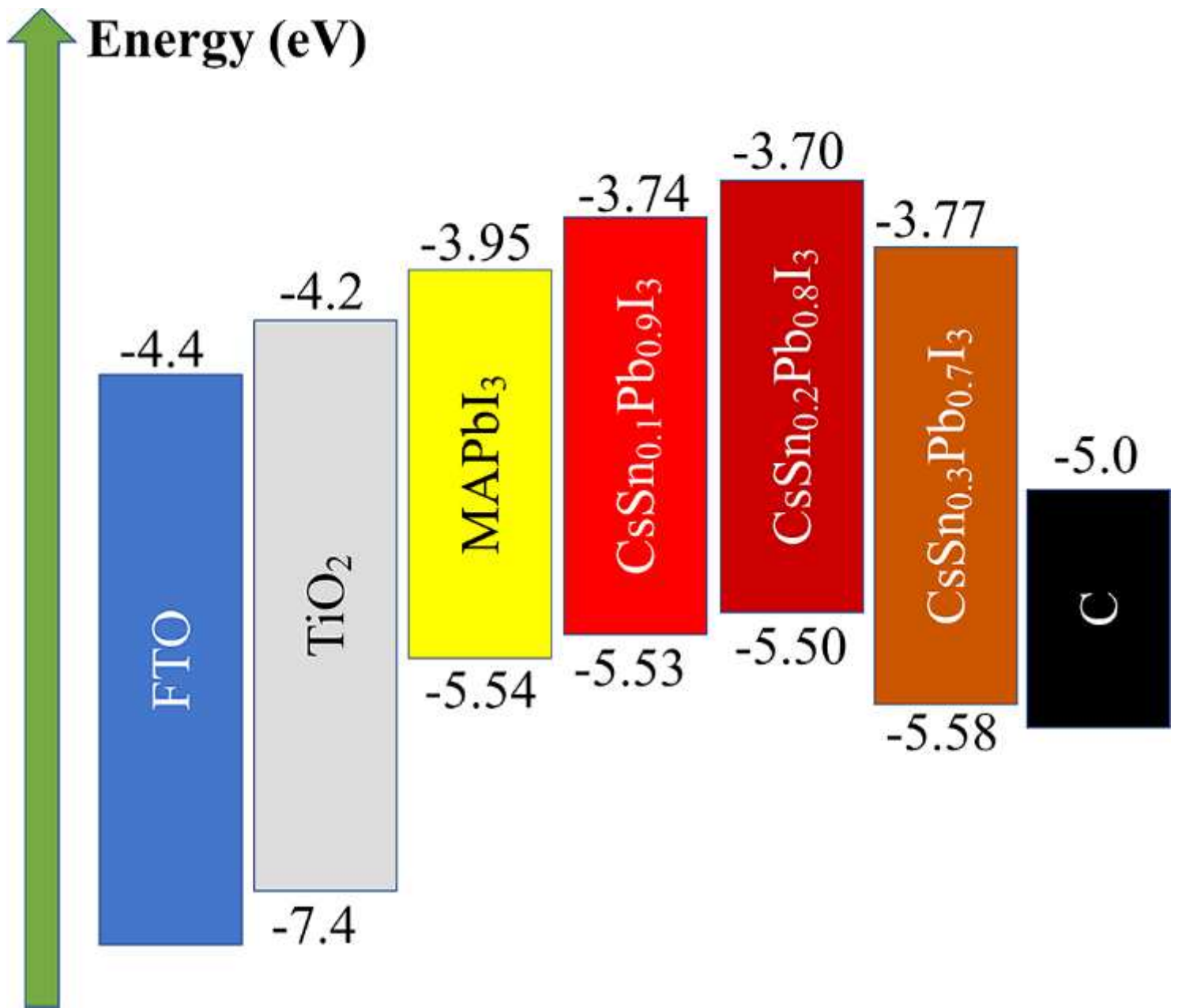


Figure 4

Band structures of different materials in PSCs

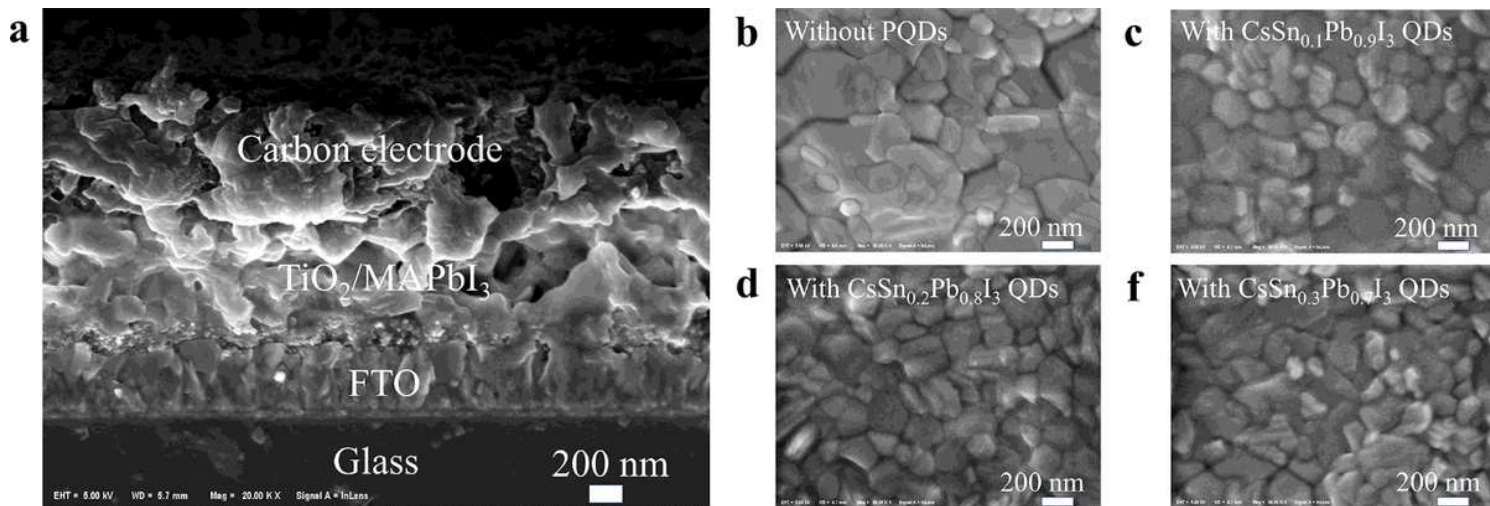


Figure 5

a Cross-sectional image of the PSC. b-f Perovskite films without and with tin-doped PQDs.

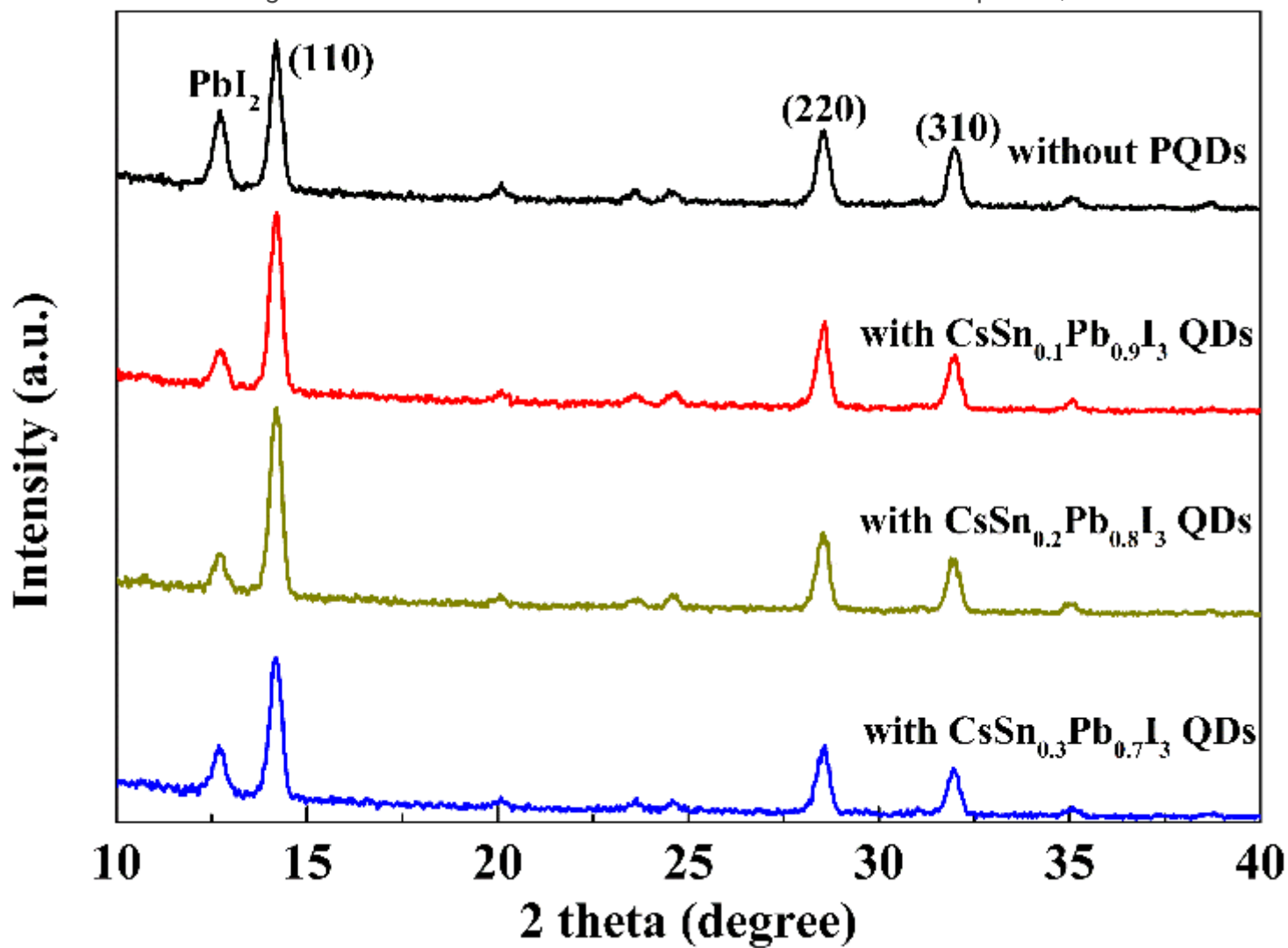


Figure 6

GIXRD patterns of different perovskite films

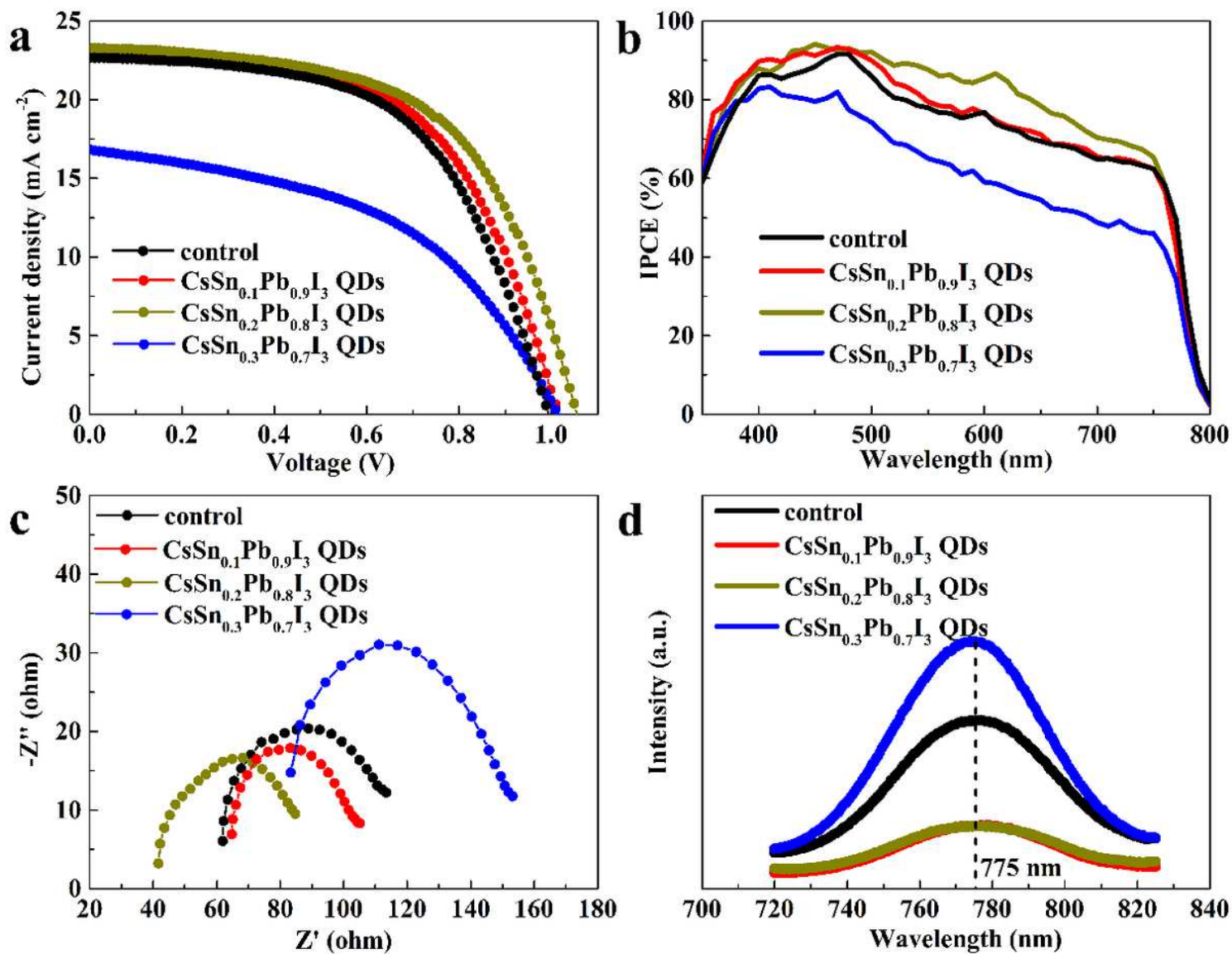


Figure 7

a J-V curves, b IPCE spectra and c EIS measurements of different PSCs. d PL spectra of perovskite films with and without tin-doped PQDs.

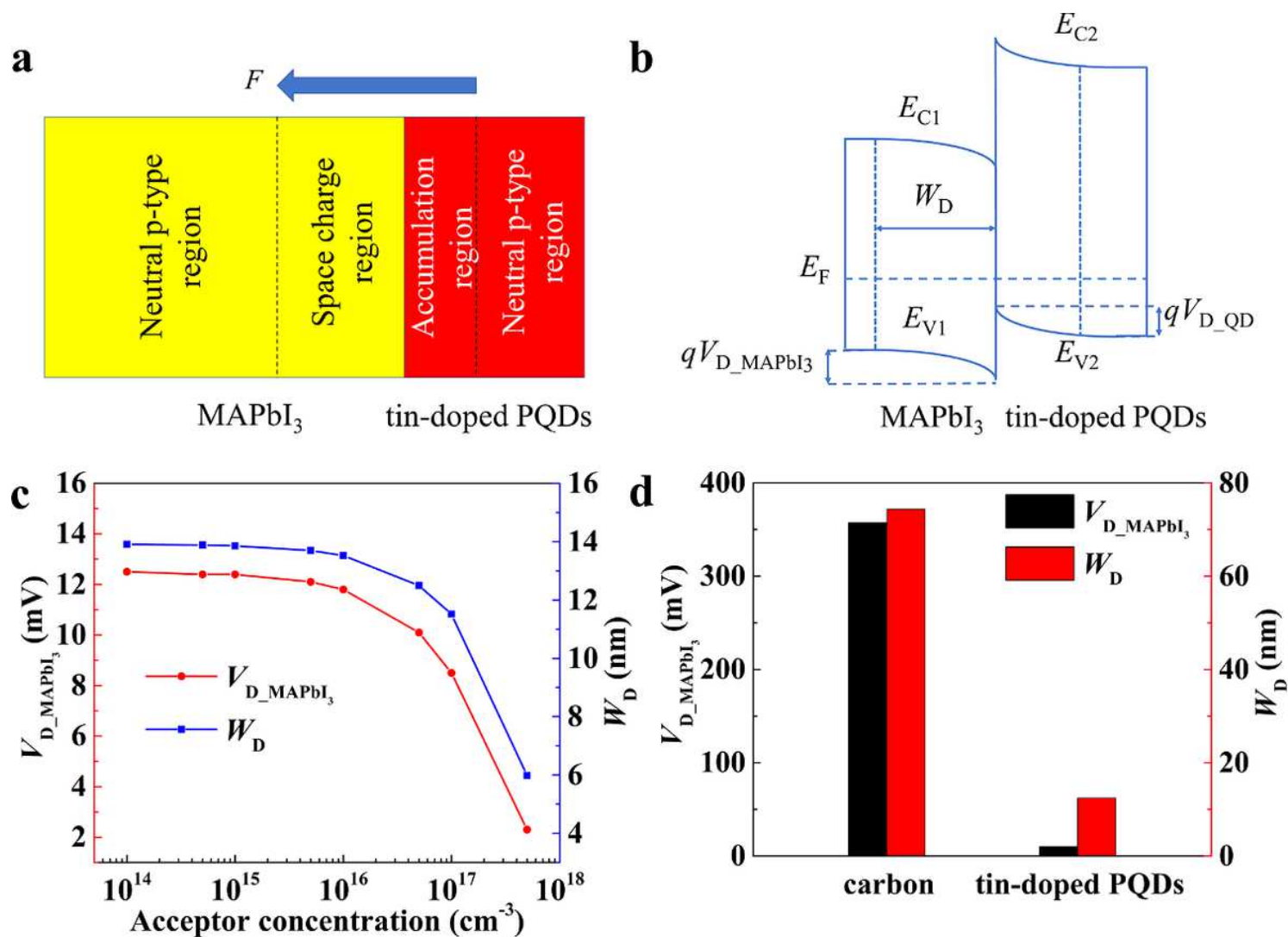


Figure 8

a The one-dimensional MAPbI₃/PQDs heterojunction model. b Corresponding energy-band diagram under the equilibrium condition. c and d Simulation results for MAPbI₃/PQDs and MAPbI₃/carbon heterojunctions.

Supplementary Files

This is a list of supplementary files associated with this preprint. Click to download.

- [NRLsupplementarymaterial.docx](#)